

# Intrinsic light reflection of conjugated films towards high-performance organic solar cells

Received: 27 May 2025

Accepted: 27 November 2025

Published online: 23 December 2025

Check for updates

Zichao Shen<sup>1,2</sup>, Guanyu Lu<sup>2</sup>, Xian Tang<sup>2</sup>, Yuanyuan Zhang<sup>3</sup>, Songqiao Li<sup>2</sup>, Jin Wang<sup>3</sup>, Jinde Yu<sup>2</sup>, Fan Gao<sup>1</sup>, Laju Bu<sup>2</sup>, Xin Chen<sup>2</sup>, Yuanwei Zhu<sup>2</sup>✉, Hongge Pan<sup>1</sup>✉, Lingxian Meng<sup>3</sup>✉ & Guanghao Lu<sup>2</sup>✉

In organic solar cells (OSCs), which represent a quintessential application system for organic conjugated films, the intrinsic light reflection of these films significantly influences the optical performance of the devices through the Fabry–Pérot micro-cavity effect. However, this phenomenon has not been comprehensively investigated. This study demonstrates that the film's intrinsic reflection arises from the light-matter interaction, which is mainly governed by the polarizability of delocalized electron cloud and the orientation of the conjugated backbone. Furthermore, the multi-level interference within the OSC micro-cavity leads to a dependence of both the reflection properties and the short-circuit current density ( $J_{sc}$ ) on the active layer thickness. Based on these insights, a strategy for synergistic optimization of device performance through precise tailoring of optical constants and the micro-cavity structure is proposed. By systematically analyzing the intrinsic reflection behavior of organic conjugated films, this study enhances the understanding of the role reflection plays in the performance of photovoltaic devices and provides theoretical support for further optical optimization of organic photovoltaics.

Organic optoelectronic devices based on organic semiconductor materials have garnered widespread attention over the past few decades due to their advantages of flexibility, solution processability, semi-transparency and low cost<sup>1–4</sup>, making them as a crucial focus in the development of next-generation electronic devices. The rapid advancement of novel organic materials has propelled notable progress in device performance. However, to further exploit the full potential of the devices, fine-tuning the optical properties of organic semiconductor films is also a critical strategy and a variety of approaches have been proposed to enhance the light utilization in such devices. For instance, the Fabry–Pérot micro-cavity effect based on multiple thin films<sup>5–7</sup> is a particularly effective approach for achieving purer color characteristics and higher light-out-coupling

efficiencies in organic optoelectronics, which is primarily attributed to the combination of two-beam or multi-beam interference effects. These effects have been extensively investigated in micro-cavity organic light-emitting diodes and other optoelectronics<sup>8–11</sup>. Generally, it occurs when the active layer with sub-micrometres thickness is sandwiched between a high-reflection metal electrode and a low-reflection metal electrode.

Organic solar cells (OSCs), as a class of prominent highly photo-sensitive organic optoelectronic devices, have achieved great development in materials designing and device optimization, boosting the power conversion efficiencies (PCEs) over 20%<sup>12–15</sup> and edging closer industrialization expectations. However, according to Shockley–Queisser (S-Q) limit<sup>16,17</sup>, the PCEs of OSCs still far from the

<sup>1</sup>Institute of Science and Technology for New Energy, Xi'an Technological University, Xi'an, China. <sup>2</sup>Frontier Institute of Science and Technology, School of Chemistry, and State Key Laboratory of Electrical Insulation and Power Equipment, Xi'an Jiaotong University, Xi'an, China. <sup>3</sup>School of Materials Science and Engineering, Zhengzhou University, Zhengzhou, China. ✉e-mail: [zhuyuanwei@xjtu.edu.cn](mailto:zhuyuanwei@xjtu.edu.cn); [honggepan@zju.edu.cn](mailto:honggepan@zju.edu.cn); [lxmeng@zzu.edu.cn](mailto:lxmeng@zzu.edu.cn); [guanghao.lu@mail.xjtu.edu.cn](mailto:guanghao.lu@mail.xjtu.edu.cn)

theoretical value. In addition to the widely discussed voltage losses, the photocurrent losses also have a significant impact on the PCEs. For example, in the D18:Z8:L8-BO based ternary OSCs, the maximum theoretical short-circuit current density ( $J_{SC, SQ}$ ) can reach  $31.8 \text{ mA cm}^{-2}$  with a band gap of  $1.43 \text{ eV}^{14}$ , while the experimental  $J_{SC}$  of the device is  $27.2 \text{ mA cm}^{-2}$ , indicating a 15% loss of the incident photon, which mainly arises from the internal quantum efficiency (IQE) loss, the parasitic absorption loss in the interlayer and the electrodes, and the reflection loss from the devices<sup>14,18</sup>. Among the various losses, the reflection losses constitute the largest proportion and strongly correlated to the optical micro-cavity effect. Typically, the incident light first passes through the transparent electrode (e.g., ITO) and then penetrates the active layer to reach a thick highly reflective bottom metal electrode (e.g., Ag), forming an optical micro-cavity<sup>10</sup>. Such a micro-cavity is crucial for regulating the light absorption and reflection, thereby optimizing both the current and PCE of the devices.

Generally, the optical micro-cavity effect essentially arises from the interference behavior of multiple reflections, and the reflection at a planar interface is primarily determined by the difference in refractive index  $n$  between the two optical mediums. When the difference is minimal, the reflection is effectively suppressed. Conversely, a substantial refractive index difference could lead to a pronounced reflection<sup>19,20</sup>. Regarding organic semiconductor films, our previous work, together with other studies, have demonstrated that they exhibit wavelength-dependent refractive indices, resulting in a strong dispersion reflection at the interface formed with the air/metal<sup>21–23</sup>. Typically, the modulation for such reflection relies on empirical external strategies, such as morphology modulation, anti-reflection layer modulation<sup>24–26</sup>, etc. However, to our knowledge, there has been a lack of in-depth research on modulating the intrinsic reflection of the organic materials layers for device optimization. Early work by Petersson et al.<sup>27</sup> modeled the photocurrent action spectra in fullerene-based OSCs by incorporating exciton diffusion and interference effects, and established a connection between the optical field distribution and charge generation. However, these models may not be directly applicable to advanced non-fullerene acceptors (NFAs) due to their distinct optical constants (refractive index  $n$  and extinction coefficient  $k$ ). Kerremans et al.<sup>20</sup> reported a method for determining optical constants from transmission spectra using the Kramers–Kronig model, yielding promising computational results. Nevertheless, the relationship between the optical constants of NFAs and their molecular/aggregate structures remains unelucidated, which hinders a comprehensive understanding of the intrinsic reflective properties of the thin films, ultimately causing targeted manipulation of the optical micro-cavity to reach a bottleneck.

In this work, we systematically investigated the intrinsic reflection properties of organic semiconductor films. As demonstrated by the grazing incident wide-angle X-ray scattering (GIWAXS) experiments and time-dependent density functional theory (TD-DFT) calculation, the electronic polarization has an impact on the light-matter interaction in the conjugated films, leading to the intrinsically high reflection with pronounced chromatic dispersion simultaneously. Typically, the organic materials with higher reflection generally feature 2D-polarized molecular backbone and face-on molecular packing, and the film reflection can be well tuned by controlling the film thickness. Subsequently, the representative PM6:Y6 based OSCs were employed to reassess the rationality of active layer thickness optimization according to the characteristic reflection property of the PM6:Y6 blend films. The total absorption/reflection of the OSCs with varying active layer thicknesses evolves from stage I to IV: thin-film bottom reflection, interference transition, thick-film interference and thick-film surface reflection. Notably, the interference transition stage achieves the maximum total absorption

and the largest  $J_{SC}$ . However, with the film thickness increasing, the strong film top reflection subsequently become dominant, leading to a decline in both the total absorption and  $J_{SC}$ . Based on the experimental and simulation results, we propose a strategy to synergistically enhance device performance parameters through precise modulation of optical constants and micro-cavity. The refractive index  $n$  can be appropriately elevated by increasing the molecular in-plane polarizability and enhancing face-on packing degree, thereby reducing the optimal thickness of the active layers and facilitating balanced  $V_{OC}$ ,  $J_{SC}$ , and  $FF$  in devices, ultimately maximizing the PCE. Our study elucidates the origin of strong reflection in organic semiconductors, simultaneously providing a fundamental principle for designing light management in OSC devices.

## Results

### Origin of the high reflection of 1D- and 2D-polarized molecules

The typical conjugation polymer P3HT and the most efficient conjugation non-fullerene small molecule acceptor Y6 were selected as examples to explore the reflection properties, and the chemical structures are presented in Fig. 1a. A self-developed light reflection measurement platform was employed to collect the light reflection data<sup>23,28</sup>. The films of Y6 and P3HT were spin-coated onto the glass substrate, and based on the interference of top/bottom reflection light, the reflection intensity was optimized through precise control of film thickness. Additionally, our investigation revealed that both the film thickness and surface roughness significantly influenced the reflection phenomena. During the film-preparation processes, the choice of solvent emerges as a crucial factor. When chlorobenzene (CB) was used for film preparation, its slower volatilization rate led to markedly enhanced crystallinity of Y6 film, generating larger grains that increased diffuse reflection and consequently weakened specular reflection, as demonstrated in Supplementary Fig. 1. In contrast, when chloroform (CF) was applied, the faster solvent evaporation resulted in smoother film, thereby avoiding intense scattering. Therefore, all NFA films in this work were prepared using CF. As shown in the Supplementary Fig. 2, the maximum reflection intensity of Y6 film was achieved at a thickness of ~50 nm, and the experimental curves of film-thickness dependent reflection of Y6 film were well matched with calculated data based on transfer matrix method (TMM)<sup>27,29,30</sup>. As depicted in Fig. 1b, the reflection peaks of Y6 and P3HT were observed at 903 nm and 615 nm, respectively, with maximum reflection and chromatic dispersion index ( $R_{max}/R_{min}$ ) of 52.9% and 7.03, 24.2% and 3.53. According to Fresnel effect, when a light beam incident from air ( $n_{air}=1$ ,  $k_{air}=0$ ) into a medium with refractive index  $n$  and extinction coefficient  $k$ , the reflection can be calculated by the following

$$R = \frac{(n-1)^2 + k^2}{(n+1)^2 + k^2} \quad (1)$$

As a result of the positive correlation between  $n$  and  $R$ , Y6 film exhibits significantly higher reflection intensity compared to P3HT, consistent with trends observed in their corresponding  $n$  and  $k$  (Fig. 1c). It is believed that the absorption is correlated to light-matter interaction, thus the distinct refraction and reflection properties of different materials should also be attributed to light-matter interactions<sup>31–33</sup>.

Additionally, the TD-DFT calculations using the Amsterdam Density Functional (ADF) package (ADF 2016.107) were further performed to verify the experimental results, and the Perdew-Burke-Ernzerhof (PBE) exchange-correlations potential and double zeta polarized (DZP) Slater-type basis set were used in all the

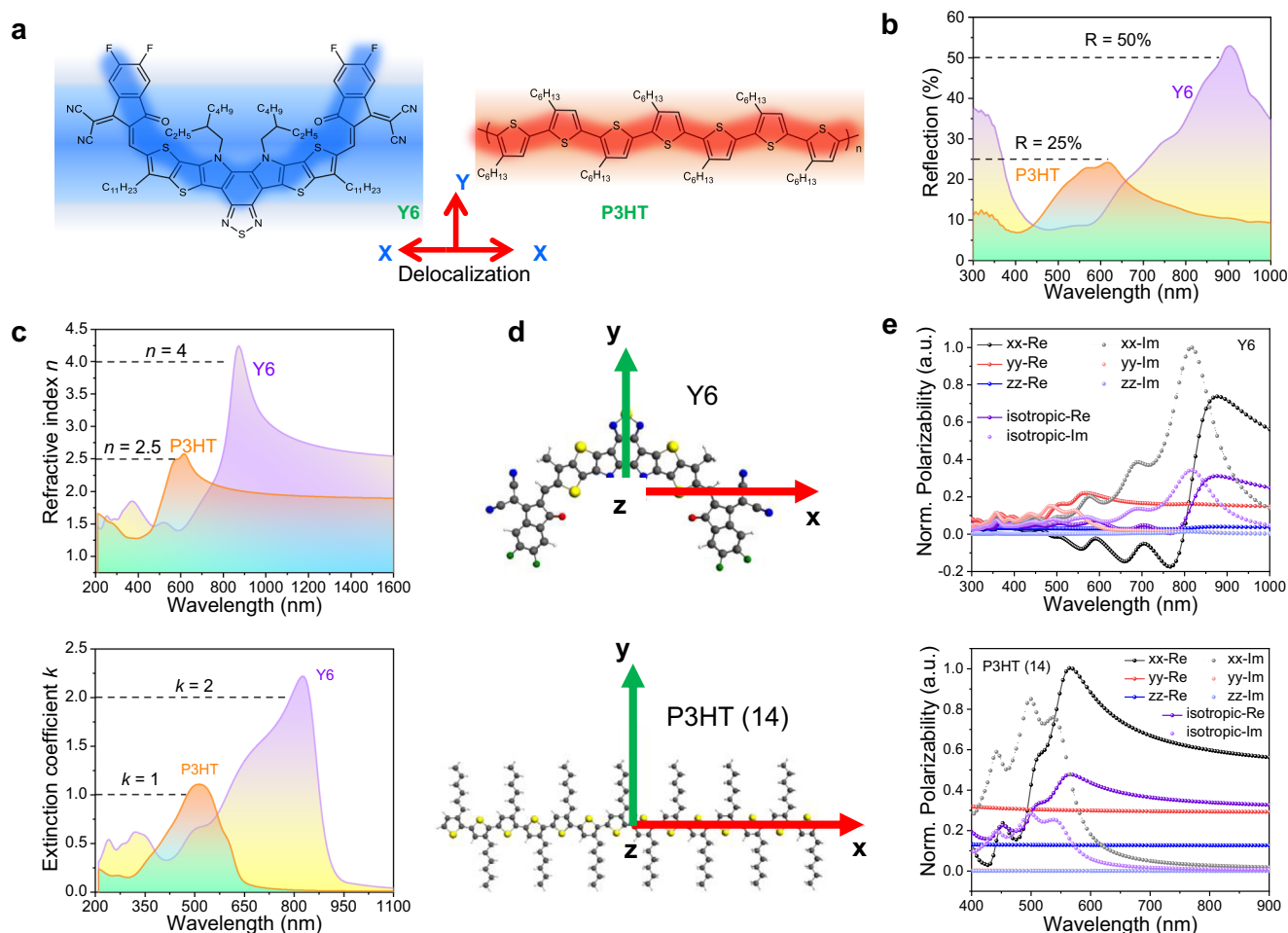


**Fig. 1 | Model organic conjugated materials investigated in this work: Y6 and P3HT and their optical characteristics.** **a** Chemical formula of Y6 and P3HT. **b** Optimized ultraviolet-visible (UV-vis) light reflection spectra of Y6 and P3HT films. **c** Plots of refractive index  $n$  and extinction coefficient  $k$  of Y6 and P3HT as a function of wavelength. **d, e** Time-dependent-density functional theory (TD-DFT)

calculation of the polarization along different directions. The “Re” in the figures represents the real part and the “Im” represents the imaginary part of the polarization. The polarization directions  $xx$ ,  $yy$  and  $zz$  refer to the coordinates as shown in **(d, e)**. AU represents arbitrary units. Source data are provided as a Source Data file.

calculations<sup>34,35</sup>. The electronic polarizability was calculated by the AORESPONSE module of the ADF program package, and in this calculation, a damping parameter  $\Gamma$  is introduced to characterize the lifetime of the excited state<sup>36</sup>. The value of  $\Gamma$  was determined by fitting the absorption spectrum of the molecule and doesn't vary significantly among molecules with similar structures<sup>37</sup>. Here, a value  $\Gamma = 0.004$  a.u. was used in all calculations of dynamic polarizability, which was obtained by fitting the absorption spectrum of the Y6 and P3HT molecules. The molecular structures and the spatial coordinates of Y6 and P3HT (14) (degree of polymerization, DP = 14) employed in the TD-DFT calculations are shown in Fig. 1d, and the corresponding calculation results are presented in Fig. 1e. The solid lines represent the real part of the electronic polarizability ( $\text{Re}(\alpha)$ ), while the dashed lines denote its imaginary part ( $\text{Im}(\alpha)$ ). The polarizability  $\alpha$ , as calculated by DFT, relates to optical constants via the dielectric constant  $\epsilon$ . By neglecting the magnetic response of the material (i.e., assuming permeability  $\mu \approx 1$ ), the square of the complex refractive index  $N$  is given by<sup>38</sup>

$$N^2 = 1 + 4\pi\rho\alpha = \epsilon \quad (2)$$

where  $N = n + ik$  is the complex refractive index,  $\alpha$  is the electric dipole polarizability, and  $\rho$  is the atomic density. The real part  $\text{Re}(\alpha)$  and imaginary part  $\text{Im}(\alpha)$  of the polarizability correspond to the dispersion

( $\epsilon_1$ ) and absorption ( $\epsilon_2$ ) components of the dielectric constant, respectively. From this equation, we observe that the variation of the refractive index real part ( $n$ ) aligns with  $\text{Re}(\alpha)$ , while the imaginary part ( $k$ ) is governed by  $\text{Im}(\alpha)$ . Moreover, an increase in  $\text{Re}(\alpha)$  enhances  $n$ , whereas a larger  $\text{Im}(\alpha)$  intensifies light absorption (higher  $k$ ).

According to the electronic polarization mechanism, the incident light will resonate with the molecules when the photoelectric field vibrates at the same frequency as the characteristic electronic vibration frequency of the molecules. Besides, different vibrations are related to different frequencies, reflecting in different wavelengths of electronic polarizability peaks. For the electronic polarizability of the P3HT (14) films, the peaks in the real part along  $X$  direction are expected to be located at 564 nm with a shoulder peak at 509 nm according to the calculation. However, the experimental reflection peaks of P3HT are observed at 615 nm and 569 nm. The blue-shift of the calculated result is primarily attributed to the interference effects presented among the during experimentation, as well as the low DP of P3HT used in calculations. Notably, the maximum polarizability occurs along the  $X$  direction, while the polarizability in  $Y/Z$  direction shows no characteristic peaks (alkyl side chain), indicating that P3HT is 1D polarization along its conjugated chain. For the Y6 films, the peaks of the electronic polarizability in the calculated real part are located at 876 nm along  $X$  direction and located at 560 nm and 503 nm along the  $Y$  direction (different vibration frequency with  $X$  direction),

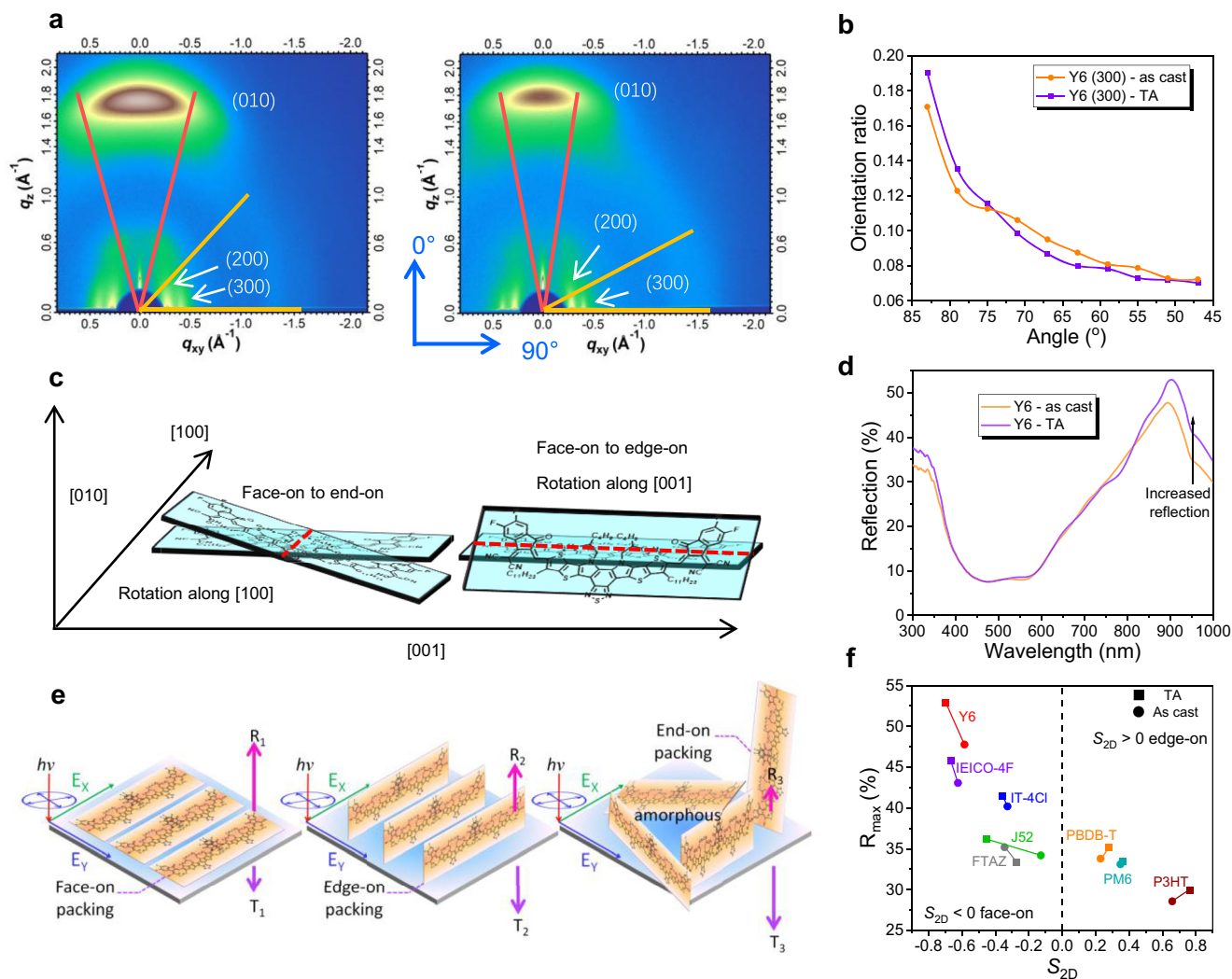


**Fig. 2 | Correlation optical reflection with molecular orientation in the film.**

**a** Grazing incident wide angle X-ray scattering (GIWAXS) pattern of Y6 before and after thermal annealing (TA) treatment. The solid lines represent diffusion range of corresponding diffractions. **b** (300) orientation ratio in the range of  $90$ – $45^\circ$  azimuth angle. After TA treatment, Y6 molecules are more uniformly aligned with the face-on orientation on substrate, which is further evidenced by other diffraction spots

shown in **(a)**. **c** Schematic diagram of declination of Y6 molecule along different directions. **d** Light absorption spectra of Y6 films before and after TA treatment. **e** Schematic diagram of relation between molecular orientation and photo-molecule interaction. **f**  $S_{2D}$  parameter versus maximum reflection ( $R_{\max}$ ) plots of classical 1D and 2D-polarized organic molecules before and after TA treatment measured in this work. Source data are provided as a Source Data file.

demonstrating the 2D-polarization of the Y6 film. Therefore, compare to the P3HT, Y6 exhibits higher reflectivity, refractive index  $n$  and extinction coefficient  $k$ .

We introduce other 1D-polarized (J52, PBDB-T, PM6, FTAZ) or 2D-polarized (IEICO-4F, IT-4Cl) molecules for statistical analysis, and the corresponding plots of refractive index  $n$  and extinction coefficient  $k$  are provided in Supplementary Fig. 3. The  $n$  values of 1D-polarized polymer are commonly lower than 3, which are obviously lower than those of 2D-polarized small molecules with  $n$  values over 3.5. The  $k$  values for these materials follow the same trend as the  $n$  values as discussed above.

Furthermore, our observations indicate that both the maximum  $n$  peak and the maximum  $R$  intensity gradually increase while undergoing a red-shift in peak positions (Supplementary Fig. 4), which may be attributed to the polarization characteristics of the materials. As reported by Hou et al.<sup>39</sup>, enhancing the electron-withdrawing capacity of molecular end groups could increase the electrostatic potential (ESP) of the molecules. The ESP reflects the degree of electron delocalization in the molecular system, where a higher ESP amplifies the radial distribution of delocalized electron clouds, thereby increasing

the polarizability, which could not only reduce the band gap and induce a redshift in absorption but also promote charge transport. Consequently, for organic semiconductors, a smaller band gap corresponds to a larger ESP and polarizability, resulting in greater optical constants, which are consistent with the statistical trend observed in our experimental measurements.

### Effect of molecular packing and orientation on reflection intensity

For organic conjugated films, the ultrahigh reflection not only originates from molecular conjugation and film thickness, but also is closely related to molecular packing orientation. As shown in the GIWAXS results in Fig. 2a, the Y6 film exhibits a distinct face-on molecular orientation, with its conjugated plane parallel to the substrate and thus perpendicular to the incident light. Furthermore, the reduced broadening of the scattering signals for the (010), (200), and (300) planes after thermal annealing (TA) treatment generally indicate improved molecular orientation uniformity<sup>40,41</sup>, and the orientation changes of Y6 molecules can be quantified by analyzing the azimuthal variation of the scattering signals. Figure 2b displays the orientation ratios of the

lamellar packing (300) plane for the Y6 film before and after TA treatment, where an azimuthal angle of 90° corresponds to the in-plane direction and 0° to the out-of-plane direction. After TA treatment, the increased ratio at larger azimuthal angles (closer to 90°) and the decreased ratio at smaller azimuthal angles (closer to 0°) demonstrate a higher degree of face-on orientation, revealing enhanced molecular order and crystallinity. As shown in Supplementary Fig. 5, the same phenomenon is observed in the GIWAXS results of other materials before and after TA treatment.

Molecular orientation changes result from rotation along different axes, which in turn leads to variations in light-matter interactions. As illustrated in Fig. 2c, for the Y6 molecular packing configuration after TA treatment, the rotation along the [100] axis induces a “face-on to end-on” orientation transition, while rotation along the [001] axis produces a “face-on to edge-on” transition. For 2D-polarized molecules like Y6, “face-on to end-on” rotation reduces the polarizability projected onto the *X*-*Y* plane, thereby weakening light-matter interactions and thus decreasing the reflection intensity. In contrast, for “face-on to edge-on” rotation, the reflection of the molecules is relatively less affected, though still influenced, because the polarizability along the *Y*-direction is much smaller than that along the *X*-direction. For 1D-polarized molecules like P3HT, “face-on to end-on” rotation also reduces the polarizability projected onto the *X*-*Y* plane, consequently diminishing light-matter interactions. However, due to their 1D-polarization characteristics, “face-on to edge-on” rotation has a negligible effect on light-matter interactions. Besides, regardless of 1D- or 2D-polarization, after TA treatment, most conjugated organic small molecules exhibited an enhanced reflection, and the corresponding reflection curves before and after TA treatment are plotted in Supplementary Fig. 6, where the TA treatment (160 °C, and higher annealing temperature will affect the composition and flatness, as shown in Supplementary Fig. 7) helps suppress the molecular rotation. As shown in Fig. 2d, the maximum reflection of Y6 is increased from 46.7% to 52.9% after TA treatment, and the maximum refractive index *n* is also increased from 4.08 to 4.17 (Supplementary Fig. 8).

In fact, based on their molecular structures, polymer donor materials such as PM6 and PBDB-T possess a certain degree of 2D-polarizability. However, their optical constants are nearly identical in magnitude to those of 1D-polarized molecules like P3HT. This phenomenon can be partly attributed to their weaker 2D-polarization characteristics compared to molecules with extended 2D-conjugation, such as Y6. Additionally, these polymers tend to adopt edge-on/isotropic molecular packing orientations, where the molecular *y*-axis remains perpendicular to the electric field vector of incident light. Consequently, polarization along the *y*-direction remains inactive, resulting in optical properties that more closely resemble those of 1D-polarized molecules.

The correlation between molecular packing within the film and the film's absorption/reflection is illustrated in Fig. 2e. For 2D-polarized small molecules like Y6, the high maximum reflection primarily stems from their highly ordered face-on orientation. As mentioned earlier, edge-on rotation causes a slight reduction in the film's reflection, while end-on rotation leads to a more pronounced decrease. The  $S_{2D}$  parameter, calculated using the formula  $S_{2D} = 2(\cos^2\gamma) - 1$ <sup>32</sup>, can be employed to quantify the degree of out-of-plane orientation from GIWAXS measurements, where  $\gamma$  represents the angle between the molecular backbone plane and the substrate plane normal. An  $S_{2D}$  value between -1 and 0 indicates a preferred face-on orientation, a value between 0 and 1 indicates a preferred edge-on orientation, and  $S_{2D} = 0$  represents an isotropic orientation. We selected the lamellar packing scattering signals, specifically the (100) plane or its higher-order diffraction for  $S_{2D}$  calculation for the following reasons: (1) The lamellar packing signals are strong and highly reliable, whereas the scattering signals from the (001) plane, which directly indicates end-on orientation, are generally difficult to observe;

(2) Improved lamellar packing uniformity leads to a reduction in isotropic molecules, which then infers to a suppression of the end-on oriented molecules that are the primary factor in reflection degradation, thereby resulting in the enhancement of film reflection<sup>40,42</sup>. (3) For molecules like Y6 that feature a three-dimensional network-like packing structure, rotation of the lamellar packing plane also implies an increase in the proportion of “end-on” oriented molecules<sup>41</sup>. We systematically investigated a series of 1D- and 2D-polarized molecules by comparing their  $S_{2D}$  parameters and maximum reflection before and after TA, as shown in Fig. 2f. The TA treatment increases the absolute  $S_{2D}$  value for all molecules, indicating enhanced orientation uniformity, and the suppression of isotropic and end-on molecular rotation, consequently leading to improved maximum reflection. The representative 2D-polarized molecules, including Y6, IT-4Cl, and IEICO-4F, exhibit maximum reflection exceeding 40% with highly face-on orientation characteristics. In contrast, the other molecules shown in Fig. 2f demonstrate reflection below 35%, primarily due to their 1D-polarization optical properties. These results are in strong agreement with refractive index measurements.

### Film-thickness-dependent OSC device performances

Inspired by the dependence of reflection on film-thickness and wavelength, we further investigate the correlation between film-thickness-dependent reflection and device absorption in an optical micro-cavity utilizing the device architecture of ITO/PEDOT:PSS/PM6:Y6/PNDIT-F3N/Ag (Fig. 3a). To this end, a series of PM6:Y6 blend films with thicknesses ranging from 20 nm to 200 nm were fabricated using chloroform as the solvent and subsequently subjected to TA treatment at 100 °C for 5 mins, and the photovoltaic performances with the thickness of 53 nm, 75 nm, 135 nm and 212 nm are presented in Fig. 3b and Table 1. Interestingly, the  $J_{SC}$  of the four devices show an undulation behavior. The device with a 53 nm thickness of the active layer shows the lowest  $J_{SC}$  (24.99 mA cm<sup>-2</sup>) due to its unsaturated light absorption, which is understandable and generally admissible. However, the device with a 135 nm thickness unexpectedly exhibits a lower  $J_{SC}$  (25.43 mA cm<sup>-2</sup>) than those of 75 nm thickness (27.16 mA cm<sup>-2</sup>) and 212 nm thickness (26.77 mA cm<sup>-2</sup>) based devices simultaneously. Additionally, the integrated  $J_{SC}$  calculated from the external quantum efficiency (EQE) curves are summarized in Table 1 and plotted in Fig. 3c, d, which can well support this phenomenon.

As observed, when the active layer thickness is too thin, the insufficient light absorption will result in a lower  $J_{SC}$ . Conversely, when the thickness exceeds 200 nm, the  $J_{SC}$  typically decrease as well due to the diminished charge dissociation and poorer charge collection properties<sup>43,44</sup>. Generally, as the active layer thickness increasing, the  $J_{SC}$  is expected to rise initially before decreasing, and the optimized thickness anticipated to be in the range of 80–120 nm. Furthermore, the photocurrent density ( $J_{ph}$ ) versus effective voltage ( $V_{eff}$ ) plots were measured to explore the charge dynamics in devices with various thickness of the PM6:Y6 blend films<sup>45</sup>.  $J_{ph}$  is calculated as  $J_{ph} = J_L - J_D$ , where  $J_L$  and  $J_D$  represent the photocurrent densities under light and dark conditions, respectively.  $V_{eff} = V_0 - V$ , where  $V_0$  is the voltage at which  $J_{ph} = 0$  and  $V$  is the external applied voltage. The probabilities of the charge dissociation ( $P_{diss}$ ) and charge collection ( $P_{coll}$ ) were calculated as the ratios of  $J_{ph}$  to the saturated photocurrent density ( $J_{sat}$ ) under short-circuit and maximum output conditions, respectively. As shown in Fig. 3e, for the devices with thickness of 53 nm, 75 nm, 135 nm and 212 nm, the  $P_{diss}$  values are 95.6%, 95.8%, 93.4% and 93.4%, respectively, indicating efficient charge dissociation in the four devices. In other words, the charge dissociation is not significantly affected by active layer thickness. However, the  $P_{coll}$  values are 86.7%, 87.0%, 83.5% and 80.1% for the respective devices, demonstrating a strong dependence of charge collection on the active layer thickness. Notably, carrier recombination and transport significantly influence the FF, reflected in  $P_{coll}$  and current density at maximum power ( $J_{Pmax}$ ). As the

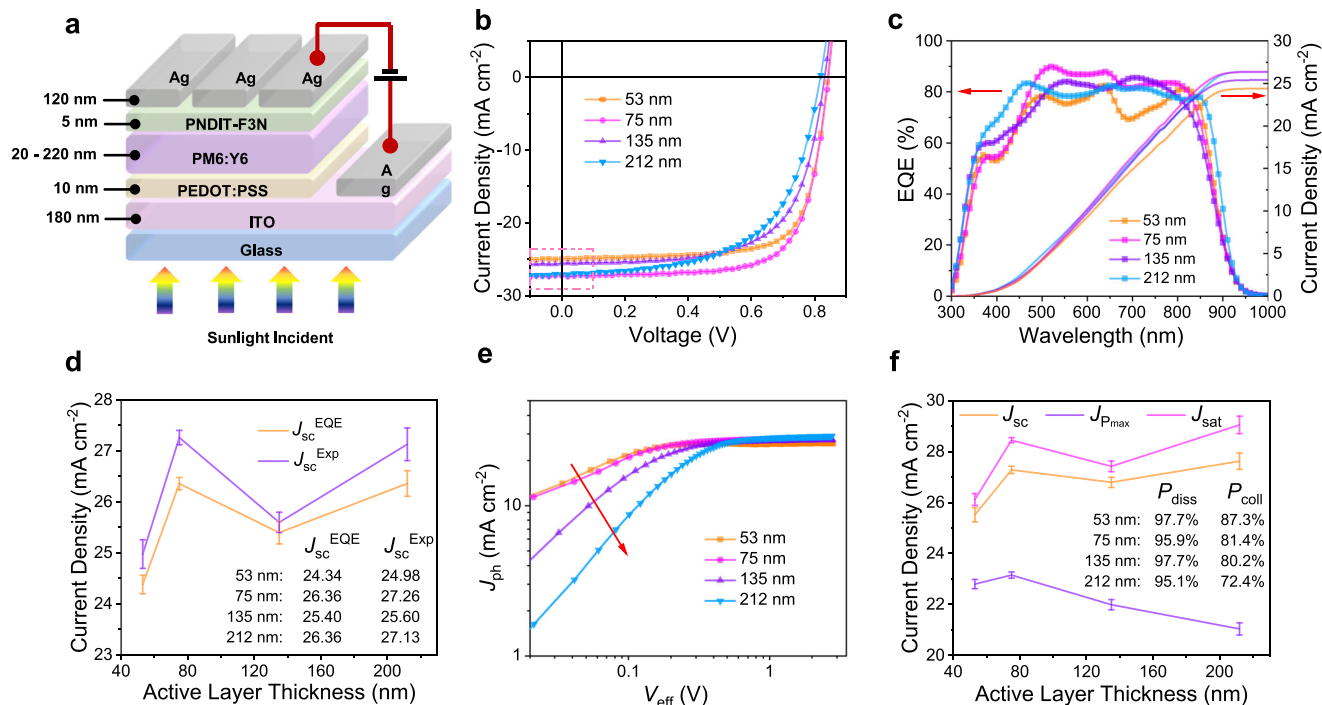


**Fig. 3 | Photovoltaic performance of PM6:Y6 devices and the dependence of  $J_{sc}$  on film thickness.** **a** Configuration of PM6:Y6 photovoltaic device. **b**  $J$ - $V$  curves and **c** External quantum efficiency (EQE) plots of PM6:Y6 based devices with different active layer thickness. **d** Film-thickness-dependence of  $J_{sc}$  from  $J$ - $V$  curves and EQE profiles, and devices with 135 nm active layer thickness shows an ineligible  $J_{sc}$  decrease. Error bars represent the standard deviation (10 independent devices). **e** Photocurrent density ( $J_{ph}$ ) versus effective voltage ( $V_{eff}$ ) plots of PM6:Y6 based devices with different active layer thickness. **f** Comparison of the evolution of  $J_{sc}$ ,

current density at maximum power ( $J_{Pmax}$ ) and saturated photocurrent density ( $J_{sat}$ ) with different active layer thickness, and the corresponding charge dissociation probabilities ( $P_{diss}$ ) and charge collection probabilities ( $P_{coll}$ ) calculation. Error bars represent the standard deviation (10 independent devices). These device characterization results confirm the existence of the film-thickness dependent  $J_{sc}$  variation, and prove that it is not attributed to the charge dissociation. Source data are provided as a Source Data file.

**Table 1 | Summarized parameters of PM6:Y6 based devices with different active layer thickness**

Material	Active layer thickness nm	$V_{oc}$ V	$J_{sc}$ $\text{mA cm}^{-2}$	$J_{sc}^{EQE}$	FF %	PCE <sup>*</sup>
PM6:Y6	53 ± 1	0.838 ± 0.004	24.99 ± 0.28	24.38	73.9 ± 0.6	15.23 ± 0.17
	75 ± 1	0.840 ± 0.004	27.16 ± 0.14	26.36	71.8 ± 0.8	16.27 ± 0.27
	135 ± 1	0.827 ± 0.005	25.43 ± 0.20	25.40	65.1 ± 0.6	13.69 ± 0.32
	212 ± 1	0.821 ± 0.003	26.77 ± 0.32	26.36	58.8 ± 0.8	12.97 ± 0.29

\*All device parameters are averaged by 10 devices.

thickness increasing from 75 nm to 135 nm, the  $P_{coll}$  decreases slightly, and further thickening to 212 nm causes a pronounced reduction in  $P_{coll}$ , indicating the recombination exacerbated with the increased film thickness, thereby degrading FF. The variations of  $J_{sc}$ ,  $J_{Pmax}$ , and  $J_{sat}$  with active layer thickness are extracted from  $J_{ph}$ - $V_{eff}$  curves and plotted in Fig. 3f. The similar trends of  $J_{sat}$  and  $J_{sc}$  provide compelling evidence that the fluctuations of experimental  $J_{sc}$  are not attributed to charge dissociation (IQE or light utilization efficiency) but rather arise from the difference light absorption and reflection.

### Charge transfer and recombination kinetics and film-depth-dependent probing

To further estimate the effect of charge transfer on carrier collection, the well-recognized ultrafast spectral transfer kinetic characterization, femto-second transient absorption (fs-TA) was subsequently conducted to gain deeper insights<sup>46</sup>. As shown in the contour maps of Fig. 4a, the negative signals at -630 nm and -807 nm correspond to the

ground state bleaching (GSB) signals of PM6 and Y6, respectively, and the positive signal at -675 nm is assigned to the excited state absorption (ESA)<sup>47</sup>. The 75 nm-thick film presents the highest  $\Delta A$  signal intensity, indicating the strong absorption of the ground state PM6 and Y6, while the 135 nm-thick film shows the lowest  $\Delta A$  signal intensity. Besides, the variation in absorption intensity at -750 nm can be attributed to fluctuations in film-thickness dependent reflection, resulting in the absorption enhancement or deterioration. However, no significant differences in exciton lifetime are evident in the contour maps. Therefore, a fitting of exciton lifetimes was subsequently performed to elucidate the ultrafast kinetics of TA spectra, as illustrated in Fig. 4b and Supplementary Fig. 9. According to the triexponential function, three lifetimes ( $\tau$ ) can be derived for each decay, where  $\tau_1$  represents the ultrafast exciton dissociation at the PM6/Y6 interface,  $\tau_2$  is related to the exciton diffusion time toward the interfaces before dissociation, and  $\tau_3$  reflects the reflection of the dynamics of free charges<sup>48</sup>. The similar  $\tau_1$  values for films of varying thickness at both

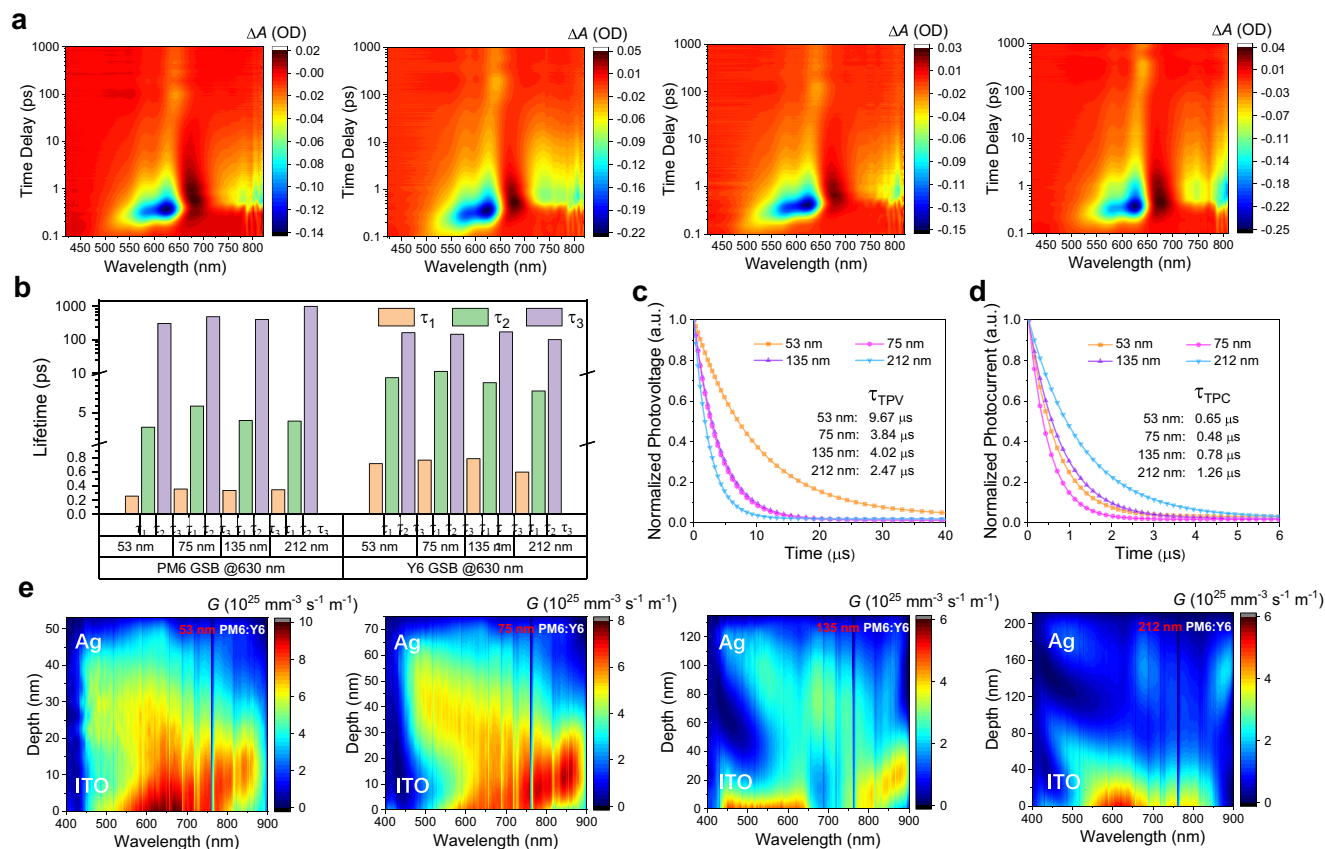


**Fig. 4 | Charge recombination characterization and film-depth dependent probing.** **a** Contour map of femto-second transient absorption (fs-TA) results of PM6:Y6 devices with different active layer thickness. **b** Exciton lifetimes of PM6:Y6 devices with different active layer thickness extracted from ground state bleaching (GSB) signals at 630 nm and 807 nm for PM6 and Y6, respectively. **c** transient photovoltage (TPV) and **d** transient photocurrent (TPC) measurement results and

the corresponding fitted lifetimes of PM6:Y6 devices with different active layer thickness. **e** Contour map of film-depth-dependent exciton generation rate simulated from the film-depth-dependent light absorption spectroscopy (FLAS) measurements. The “vertical-lines” in the contour are due to the characteristic of AM1.5G solar spectra. Source data are provided as a Source Data file.

630 and 807 nm corroborate the similar ultrafast hole/electron transfer at the interfaces, except that of 53 nm films at 630 nm, which is slightly shorter than others, indicating the more efficient hole transfer of 53 nm films. Comparing to the other film, the prolonged  $\tau_2$  for the 75 nm film at both 630 and 807 nm can be attributed to the extended exciton diffusion length, which is beneficial for suppressing charge recombination and enhancing the  $J_{SC}$  and FF<sup>49</sup>. However, the strong built-in voltage under short-circuits conditions (the sufficiently large  $V_{eff}$ ) is capable to weaken the effect of exciton diffusion length<sup>50,51</sup>, while the FF corresponds to the maximum output power conditions is more sensitive to the exciton diffusion distance. In addition,  $\tau_3$  values for all the films of different thicknesses fall within the same order of magnitude, suggesting minimal impact on device current density, especially under short-circuits conditions.

Moreover, the transient photovoltage (TPV) and transient photocurrent (TPC) are subsequently measured to further illustrate the charge recombination kinetics<sup>52,53</sup>, and the corresponding lifetime simulation results are provided in Fig. 4c, d. Note that device with 212 nm active layer thickness shows shorter photovoltage decay lifetime (2.47  $\mu$ s) and longer photocurrent decay lifetime (1.26  $\mu$ s) than those of other devices with thinner active layer thicknesses, suggesting the enhanced recombination in the 212 nm thickness-based device, thus resulting in the reduced FF values. On the other hand, the device with the thinnest film thickness of 53 nm shows the longest photovoltage decay lifetime (9.67  $\mu$ s) and relatively short photocurrent decay lifetime (0.65  $\mu$ s), indicating that the weakest

charge recombination in 53 nm thick devices<sup>50</sup>. The shorter photocurrent lifetime (0.48  $\mu$ s) observed in the 75 nm film compared to the 135 nm film (0.78  $\mu$ s) arises from reduced carrier drift distance due to the thinner active layer, enabling faster charge collection. Moreover, the carrier mobility is another possible affecting factor on experimental  $J_{SC}$ , therefore the photo-induced charge carrier extraction in linearly increasing voltage (photo-CELIV) measurement was afterwards performed<sup>54,55</sup>. As shown in Supplementary Fig. 10, the calculated carrier mobilities of the devices with 53 nm, 75 nm, 135 nm and 212 nm active layer thickness are  $2.29 \times 10^{-5} \text{ cm}^2 \text{ V}^{-1} \text{ s}^{-1}$ ,  $6.12 \times 10^{-5} \text{ cm}^2 \text{ V}^{-1} \text{ s}^{-1}$ ,  $1.59 \times 10^{-4} \text{ cm}^2 \text{ V}^{-1} \text{ s}^{-1}$  and  $1.44 \times 10^{-4} \text{ cm}^2 \text{ V}^{-1} \text{ s}^{-1}$ , respectively. Therefore, the slightly prolonged photocurrent lifetime in the 53 nm film primarily stems from a notable decline in carrier mobility.

However, under short-circuit conditions, the built-in electric field is sufficiently strong to substantially suppress carrier recombination. When recombination's impact on  $J_{SC}$  is negligible, minor variations in carrier mobility exert limited influence on collection efficiency. The dominant factor affecting  $J_{SC}$  remains the  $P_{diss}$ , which is ranging between 93% and 96%, leading to minimal influence on the observed trends in  $J_{SC}$  and  $J_{sat}$ . In summary, the subtle differences in carrier dynamics minimally impact  $J_{SC}$ , as confirmed by the experimentally observed thickness-dependent trends of  $J_{SC}$  and  $J_{sat}$ . This further underscores that the variation in  $J_{SC}$  predominantly originates from optical absorption differences, given the comparable  $P_{diss}$  across thicknesses.

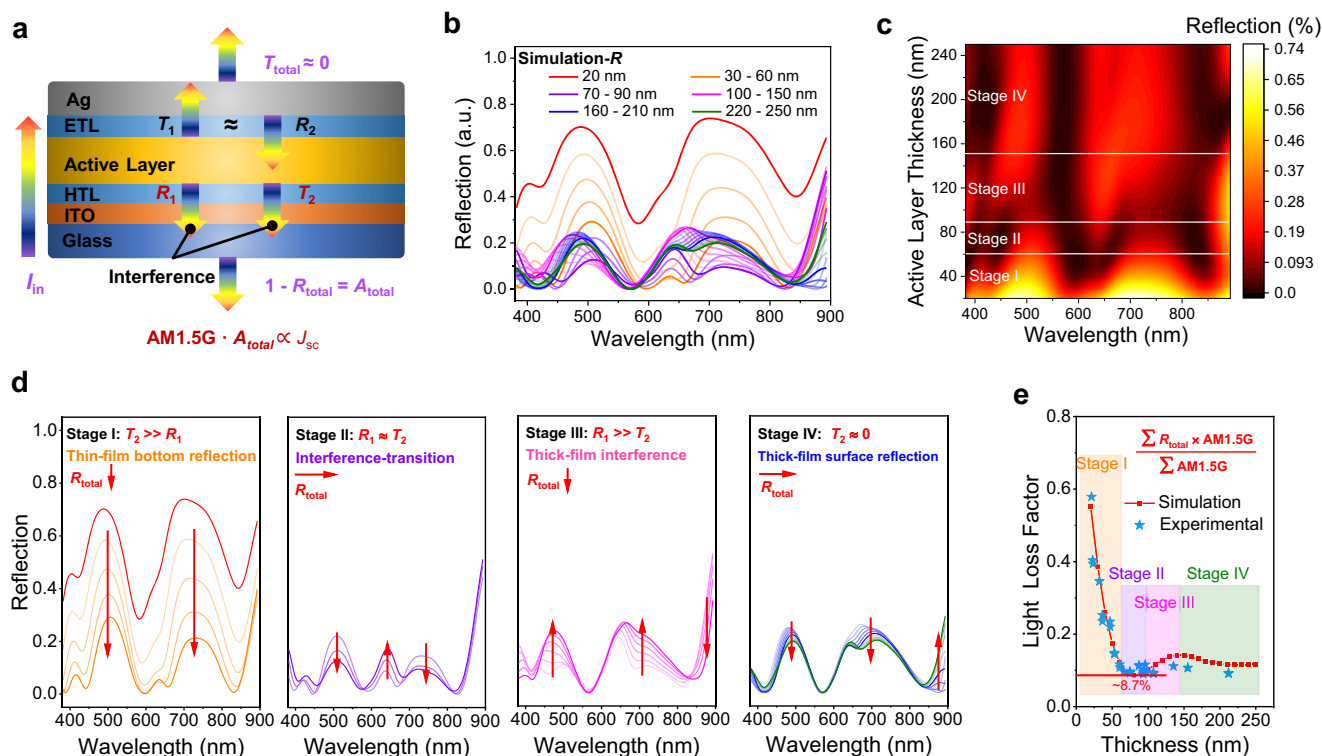


**Fig. 5 | Modulation, simulation and experimental measurements of total reflection of PM6:Y6 based devices with different active layer thickness.**

**a** Schematic diagram of device light path. For opaque devices with 120 nm Ag electrodes, the  $R_2$  can be considered as equal to  $T_1$ . **b** Simulation results of device total reflection with the variation of active layer thickness. AU represents arbitrary units. **c** Contour map of device total reflection with the variation of active layer

thickness. From **b, c**, the strong interference can be observed in the film-thickness range of 70–210 nm. **d** Stage I to IV separated from **b, c** according to the change of the relationship between  $T_2$  and  $R_1$ . The red arrows indicate the trend. **e** Simulated and experimental light loss factors of devices with different active layer thickness. Source data are provided as a Source Data file.

Additionally, we observed that the series resistance ( $R_s$ ) increases linearly with film thickness beyond 75 nm under dark conditions, indicating that contact resistance is insensitive to film thickness and morphology ( $0.41 \pm 0.08 \Omega \cdot \text{cm}^2$ )<sup>56</sup>, as shown in Fig. S11 and Table S1. Concurrently, a monotonic increase in shunt resistance ( $R_{sh}$ ) with thickness was observed, demonstrating that thicker films effectively suppress pinhole effects, thereby reducing device leakage current. Generally, Higher  $R_s$  and lower  $R_{sh}$  could both lead to a reduction in  $J_{SC}$ , and these resistive characteristics confirm that the 75 nm-thick PM6:Y6 device achieves the optimal balance of  $R_s$  and  $R_{sh}$ , which aligns with its highest PCE. Critically, interfacial contact is not the primary cause of the reduced  $J_{SC}$  in the 135-nm device.

Furthermore, vertical phase separation may also affect the  $J_{SC}$  of the device by adjusting the distribution of the optical electric field. To isolate this effect, we investigated the influence of vertical phase separation on the  $J_{SC}$  of the PM6:Y6 device using the film-depth-dependent light absorption spectroscopy (FLAS) technology<sup>57,58</sup>. The calculated vertical component distribution was plotted in Supplementary Fig. 12. The distribution of 212 nm films is the most uniform while the others present analogous n-i-p configuration, which is more favorable for conventional devices. The contour maps of film-depth-dependent exciton generation rates ( $G$ )<sup>59</sup> are drawn in Fig. 4e, and the corresponding distributions of photoelectric field ( $|E|^2$ )<sup>60,61</sup> of different devices are provided in Supplementary Fig. 13, which is simulated via TMM from FLAS results. The exciton generation rates of 53 nm and 75 nm thickness films reach their maximum at the middle of the films, which possess the relatively short carrier diffusion distance and thus are beneficial to carrier collection<sup>62</sup>, while those of 135 nm and 212 nm films are concentrated at the active layer/ITO interfaces with enlarged

carrier diffusion distance. This discrepancy is mainly due to the multi-interferences between reflections at the interfaces of different optical mediums. Based on the exciton generation rates calculation, the integrated total  $G$  of the devices is plotted in Supplementary Fig. 14, along with the simulated  $J_{SC}$  values for devices with different active layer thickness. As illustrated, the integrated  $G$  is identical to the simulated  $J_{SC}$ , corroborating the trends observed in the experimental  $J_{SC}$  variation with active layer thickness.

### Principle of film-thickness dependent reflection/absorption in cell micro-cavity

Both  $J_{ph} \cdot V_{eff}$  results and ultrafast transfer/recombination kinetics characterization are insufficient to explain the observed fluctuations in  $J_{SC}$  related to film-thickness. Additionally, the surface roughness of PM6:Y6 thin films exhibits minimal variation (at least two orders of magnitude smaller than the wavelength) across different active layer thicknesses and is also not the primary factor contributing to fluctuations in  $J_{SC}$  (Supplementary Fig. 15). However, the simulations based on FLAS measurement reveal trends similar to those of the experimental  $J_{SC}$ . Consequently, we believe that the variation in total reflection, resulting from the micro-cavity effect, is the primary factor influencing the  $J_{SC}$ -thickness dependence. As demonstrated in Fig. 5a, the incident light experiences multi-level reflection, resulting in the interference device total reflection. Generally, the reflection intensity is mainly correlated with the difference in refractive index  $n$  between the two optical medium (specular reflection)<sup>63</sup>, with a larger difference typically leading to stronger reflection. Consequently, due to the significant differences in the complex

refractive index ( $n$ ,  $k$  values) of the active layer compared to the Ag electrode, ITO electrode, HTL, and ETL, as provided in Supplementary Fig. 16, the strongest reflection should occur at either HTL/active layer interface ( $R_1$ , top reflection) or at ETL/Ag bottom interface ( $R_2$ , bottom reflection), and in this case, reflections at other layer interfaces are hidden in order to a comprehensive illustration. In addition, the  $R_2$  will sequentially pass through the whole device again, contributing to the transmitted light ( $T_2$ )<sup>22,23</sup>. Given the high reflection property of the thick Ag electrode, the total transmission intensity is close to zero, implying that the total absorption of the device can be obtained by subtracting the total reflection from the incident light ( $I_{in} - R_{total}$ ). Therefore, the first transmitted light intensity ( $T_1$ ) can be considered equivalent to the bottom reflection intensity ( $R_2$ ). Thus, the competition and interference between  $R_1$  and  $T_2$  are the critical factors that determine the total reflection of OSCs devices and thus the absorption and  $J_{SC}$ .

Based on experimentally measured refractive indices of the different materials, the total reflection  $R_{total}$  of OSCs devices with different active layer thicknesses was simulated using TMM, and the thicknesses of ITO, PEDOT:PSS, PNDIT-F3N, and Ag electrode layers are strictly kept consistent with the experimental condition in the simulation. As depicted in Fig. 5b, c, the  $R_{total}$  significantly reduced as the active layer increases from 20 nm, suggesting that more incident light is absorbed. When the active layer thickness reaches ~75 nm, the strong interference effects become apparent, leading to the wavelength-dependent reflection fluctuation, and thus the  $R_{total}$  intensity is hard to be distinguished. Upon refining the evolution of  $R_{total}$  with active layer thickness, it can be categorized into four distinct stages (Fig. 5d):

**Stage I: Thin-film (<70 nm) bottom reflection (Ag/active layer interface).** During this stage, although the bottom reflection makes the incident light pass through the whole film again, the light absorption is still not close to saturation. The strong bottom reflection induced secondary transmission ( $T_2$ ) with a shape of reversed film absorption caused by unsaturated light absorption is significantly larger than the active layer top reflection ( $T_2 \gg R_1$ ). In this case,  $T_2$  plays a dominating role on the interference with  $T_2$  and  $R_1$ , and consequently the  $R_{total}$  at this stage will continuously become weaker, resulting in the increased device total absorption ( $A_{total}$ ) as well as  $J_{SC}$  of the device.

**Stage II: Interference-transition (70–90 nm).** As active layer thickness further increasing, the  $A_{total}$  gradually approaches saturation. Consequently, the interference between  $T_2$  and  $R_1$  enters a transition step, therefore, the  $R_{total}$  exhibits obvious interference characteristics. Since the optical path difference (OPD) between  $R_1$  and  $T_2$  at this circumstance is approximately an odd-multiple of half-wavelength (at PM6:Y6 absorption peak), namely the phase difference also becomes an odd-multiple of  $\pi$ , resulting in the destructive interference between  $R_1$  and  $T_2$ . Due to the similar intensity of both beams ( $R_1 \approx T_2$ ) and the destructive interference, the  $R_{total}$  intensity at this film-thickness range is minimized, and the  $A_{total}$  and  $J_{SC}$  approach their maximum values.

**Stage III: Thick-film interference (90–150 nm).** As the OPD of  $R_1$  and  $T_2$  continues to increase, closing to the half-wavelength integer multiple at the absorption peak, the two light beams will produce constructive interference, leading to a gradual increase in  $R_{total}$ . Additionally, as the thickness of the active layer increases, the intensity of  $T_2$  is further reduced ( $R_1 \gg T_2$ ), which increases the weight of  $R_1$  in the interference process, and results in an increased  $R_{total}$ .

**Stage IV: Thick-film (>150 nm) surface reflection (ITO/active layer interface).** The thick active layer is able to absorb all the incident light ( $I_{in} - R_1$ ), and the secondary transmission light  $T_2$  can be considered as zero ( $T_2 \approx 0$ ), leading to the surface dominating reflection. In this case, after experiencing a small period of constructive interference, the  $R_{total}$

approaches a fixed value, which is equal to the active layer surface reflection.

The experimental evolution of the total light loss factor with variation active layer thicknesses is provided in Fig. 5e and Supplementary Fig. 17, alongside the calculated results, with the corresponding four evolution stages emphasized. At an optimized active layer thickness of ~75 nm, the total light loss reaches ~8.7%. According to Zhu's observation<sup>14</sup>, a state-of-the-art device fabricated by the most advanced photovoltaic materials with ~20% PCEs still experiences ~15% light loss. Our experimental and theoretical findings further demonstrate that more than half of the light loss is attributed to the reflection loss, which is as a result of intrinsic chromatic dispersed light reflection property of organic conjugated films.

In addition to conventional devices, we also conducted identical studies on inverted devices with different transport layers and electrodes, as well as flexible devices with different substrates, using the PM6:Y6 system as an example, in order to verify the effect of conjugated film intrinsic light reflection on device performance. The device performance test results are shown in Supplementary Fig. S18 and Supplementary Table 3. It can be observed that both inverted and flexible devices exhibit a similar trend of  $J_{SC}$  variation with thicknesses as conventional devices (Fig. 5), indicating that minor differences in the optical constants of the transport layers, electrodes, and substrates do not significantly affect the optical performance of the devices (Supplementary Fig. S19). This conclusion is further supported by the simulated light reflection results of PM6:Y6 inverted devices with different thicknesses (Supplementary Fig. 20).

Indeed, this optical micro-cavity effect, which depends on the reflection properties of the active layer, also holds instructive significance for organic photodetectors. The responsivity of a photodetector to light of different wavelengths reflects its applicability under irradiation at various wavelengths and can likewise be modulated by adjusting the active layer thicknesses. By converting the EQE curves of PM6:Y6-based OSC devices, the photoresponsivity ( $R$ ) curves of the organic photodetectors can be obtained<sup>64,65</sup>. As shown in Supplementary Fig. 21, these curves exhibit a fluctuation trend highly similar to that of the device's reflection light (Supplementary Fig. 17). This not only confirms the decisive role of reflection light in device absorption but also offers a strategy for wavelength-selective optimization.

### Correlation between film-thickness dependent reflection and device absorption

In order to simulate the device absorption under real conditions, we carefully calculate the integrated  $A_{total}$  under AM1.5G illumination ( $Abs_{AM1.5G}$ ). Since the total transmission is close to zero, the  $A_{total}$  can be ascribed as  $1 - R_{total}$ , so the  $Abs_{AM1.5G}$  can be calculated using the following

$$Abs_{AM1.5G} = \int_{382nm}^{893nm} A_{total} \times AM1.5G \, d\lambda \quad (3)$$

where the  $A_{total}$  is simulated via TMM, and the AM1.5G is the standard reference solar radiation spectrum. The reason for choosing this wavelength range of 382–893 nm is that PM6:Y6 film only absorbs in this wavelength range, and the apparent absorption greater than this wavelength range is actually interference from the reflection light of Y6. The active layer thickness-dependent  $Abs_{AM1.5G}$  calculation results and the experimental  $J_{SC}$  results ( $J$ -Exp and  $J$ -EQE) are normalized and plotted in Fig. 6a, with corresponding values lists in Supplementary Table 2, and the experimental total reflection of devices with different active layer thicknesses are provided in Supplementary Fig. 18. All the curves in Fig. 6a experience a fluctuating process and reach a maximum in the range of 70–90 nm, which aligns with our  $R_{total}$

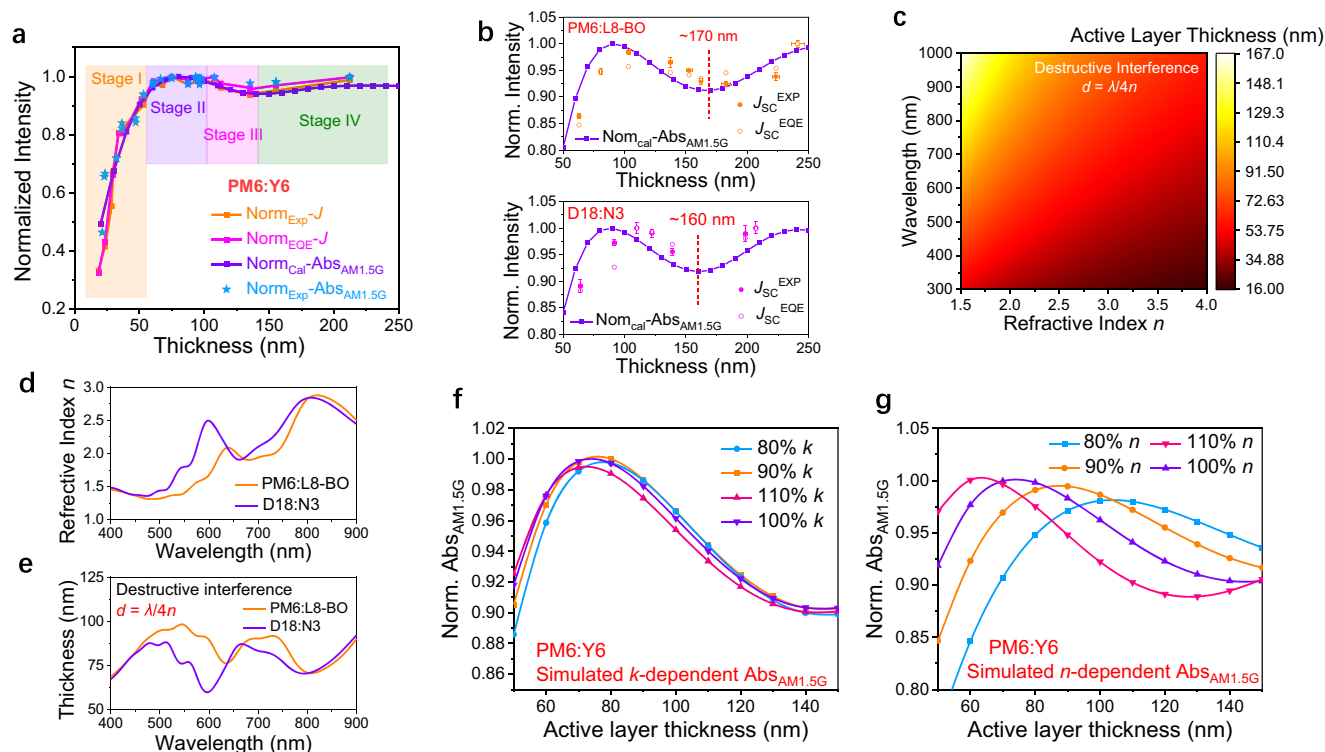


**Fig. 6 | Comparison of experimental  $J_{SC}$  results with transfer matrix method (TMM) based simulation, and the universality of film-thickness dependent  $J_{SC}$  fluctuation.** **a** Normalized calculation and experimental results of active layer thickness dependent  $Abs_{AML5G}$  and  $J_{SC}$  of PM6:Y6 devices. **b** The active layer thickness dependent experimental  $J_{SC}$  results of PM6:L8-BO and D18:N3 devices. Error bars represent the standard deviation (10 independent devices). **c** Contour

map of destructive interference wavelength for different refractive index  $n$ . **d** Refractive index  $n$  of PM6:L8-BO and D18:N3. **e** The thickness corresponds to destructive interference of PM6:L8-BO and D18:N3. **f** Simulated  $k$ -dependent and **g**  $n$ -dependent  $Abs_{AML5G}$  of PM6:Y6 devices. Source data are provided as a Source Data file.

calculations. Their high coincidence among these results means that our simulation model is reasonable and reliable.

To further prove the universality of this micro-cavity effect, two more series of devices were prepared using other state-of-the-art active layer materials D18:N3<sup>66,67</sup> and PM6:L8-BO<sup>68,69</sup>, and the corresponding  $J-V$  curves are provided in Supplementary Fig. 17. As shown in Fig. 6b, the  $J_{SC}^{Exp}$  and  $J_{SC}^{EQE}$  were extracted from  $J-V$  measurements, and the solid lines are our simulation results of  $Abs_{AML5G}$  based on TMM. Notably, The  $J_{SC}$  depressions also appeared and located at ~160 nm and ~170 nm for D18:N3 and PM6:L8-BO, respectively.

Although the configurations of OSCs devices is composed by packing multiple functional layers, the optical model of micro-cavity can be simplified as the equal thickness interference due to the large refractive indices difference between organic conjugated films and other interface layers (ITO, ETL and HTL). According to the equal thickness interference, the following equation can be used to predict the interference behaviors (when the incident angle equals to 0°)

$$2nd = \begin{cases} m\lambda & (m=1, 2, \dots) \text{ Constructive} \\ (m-0.5)\lambda & (m=1, 2, \dots) \text{ Destructive} \end{cases} \quad (4)$$

where  $\lambda$  is wavelength,  $n$  is the refractive index,  $d$  is the film thickness,  $m$  is an integer variable. Using this relationship, the thickness corresponding to the destructive interference of different binary blends with diverse  $n$  values at difference absorption peaks can be calculated as equal to  $\lambda/4n$ , as shown in Fig. 6c.

The  $n$  values of PM6:L8-BO and D18:N3 blend films are measured by ellipsometer and provided in Fig. 6d, and the calculated corresponding thicknesses to the destructive interference are plotted in Fig. 6e. As we can see, for the two systems, the refractive index  $n$  of the

acceptor absorption region is similar (~800 nm), with a maximum of around 3; however, the refractive index  $n$  of the donor absorption region varies greatly. The refractive peaks of PM6 and D18 are around 638 nm and 598 nm with the maximum refractive indices of 2.03 and 2.49, respectively.

Experimental results from PM6:Y6, PM6:L8-BO, and D18:N3 systems, combined with calculations based on the equal-thickness interference model, indicate that an increase in the  $n$  values lead to a reduction in both the optimal thickness ( $d_{opt}$ ) for  $J_{SC}$  and the thickness threshold at which  $J_{SC}$  begins to decline. However, the impact of  $n$  on absolute absorption intensity remains unclear. To address this issue, we simulated the  $Abs_{AML5G}$  of PM6:Y6 by independently varying either  $n$  or  $k$ , as shown in Fig. 6f, g. The results demonstrate that the  $k$  has negligible influence on  $d_{opt}$  for  $J_{SC}$ . However, deviations in  $k$  (either higher or lower) may reduce the maximum absorption intensity, which is likely because reflectance is jointly determined by  $n$  and  $k$ . In contrast,  $n$  plays a more dominant role: increasing  $n$  monotonically decreases  $d_{opt}$  for  $J_{SC}$ , which may facilitate synergistic optimization of  $J_{SC}$ , FF, and  $V_{OC}$ . Interestingly, reducing  $n$  not only increases  $d_{opt}$  for  $J_{SC}$  but also diminishes the maximum absorption intensity. Based on these experimental and simulation findings, we believe that a moderate increasing in  $n$  can enhance the  $J_{SC}$  and simultaneously minifying the optimal thicknesses for  $J_{SC}$ .

### Discussion on optimizing refractive index to enhance optical device performance

The microcavity effect enables the  $J_{SC}$  to attain an optimal thickness  $d_{opt}$ . However, the optimal thicknesses for FF and  $V_{OC}$  generally reside at lower values. For instance, in the PM6:Y6 system mentioned above, optimal thickness for FF is ~45 nm, for  $V_{OC}$  is ~35 nm, and for  $J_{SC}$  is ~75 nm (Fig. 7a). However, this thickness mismatch between electrical

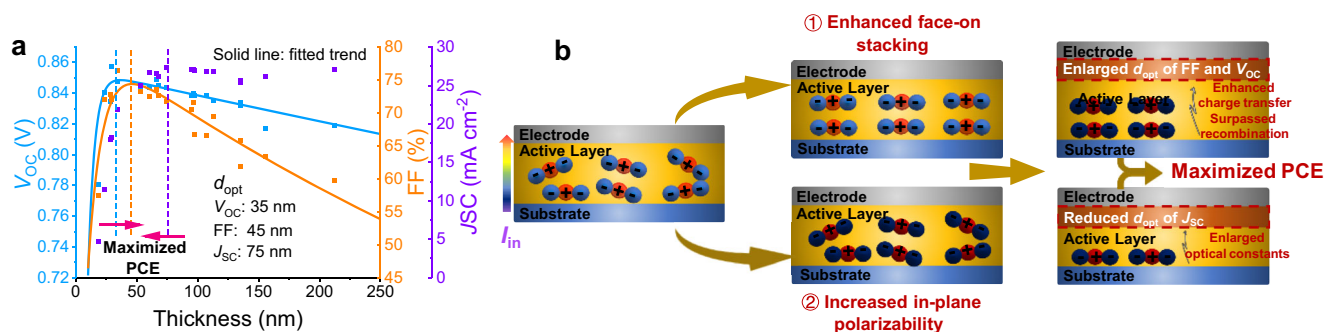


**Fig. 7 | Our proposed strategy for synergistic optimization of  $V_{OC}$ ,  $J_{SC}$  and FF.** **a** Evolution of  $V_{OC}$ ,  $J_{SC}$ , and FF in PM6:Y6 devices as a function of active-layer thickness. **b** Schematic illustration of the strategy: coordinated optimization of  $V_{OC}$ ,

$J_{SC}$ , and FF is achieved by tuning optical constants through modulation of molecular in-plane polarizability and thin-film packing orientation. Source data are provided as a Source Data file.

parameters (FF/ $V_{OC}$ ) and optical parameter ( $J_{SC}$ ) fundamentally limits device efficiency optimization.

For this dilemma situation, based on our measurements of optical constants for the PM6:Y6, PM6:L8-BO, and D18:N3 systems, combined with thickness-dependent  $J_{SC}$  and TMM-based simulations, we conclude that larger optical constants correlate with a reduced  $d_{opt}$ , which approaches the optimal thickness for maximizing FF and  $V_{OC}$ . Building on these findings, we propose the following two material design strategies to reconcile this thickness divergence, as illustrated in Fig. 7b:

- (1) Increased in-plane molecular polarizability: Strengthening electron-withdrawing capabilities at molecular terminals increases electrostatic potential, which promotes charge dissociation/transport by delocalizing electron clouds. This molecular engineering approach could shift the optimal thicknesses of FF/ $V_{OC}$  toward higher values.
- (2) Enhanced face-on orientation: Preferential face-on packing aligns molecular polarization with the optical electric field vector. This configuration simultaneously improves charge transport and reduces the optimal thickness of  $J_{SC}$  through enhancing light-matter interaction.

It is important to clarify that these two strategies are not competitive but complementary. Enhancing the in-plane polarizability of materials (for instance, through fluorinated end groups or asymmetric molecular structures) simultaneously promotes charge generation/transport and improves face-on molecular stacking<sup>70,71</sup>. This dual effect optimizes the thickness corresponding to peak performance in  $J_{SC}$ /FF/ $V_{OC}$ , thereby collectively elevating the device's PCE. This paradigm provides critical guidelines for next-generation OPV material development.

## Discussion

In this work, we systematically investigated the strong intrinsic optical reflection of organic conjugated materials and its chromatic dispersion, which is highly correlated to the polarizability of conjugated backbone and molecular stacking orientation. Notably, the materials with higher reflection materials basically feature a 2D-polarized molecular backbone and face-on molecular packing. As a typical reflection application for the classical PM6:Y6 binary OSCs, the optimal active layer thickness is estimated to be ~75 nm because the top/bottom device reflection destructive interference occurred in micro-cavity and thus the device absorption is enhanced, which was confirmed by both TMM-based simulation and experimental results after excluding the influence of roughness, contact and charge transfer/recombination. The rationality of thickness regulation of D18:N3 and PM6:L8-BO based OSCs can also be clarified by optical micro-cavity model. Subsequently, based on these experiment and simulation

results, we propose a strategy to achieve synergistic enhancement of  $V_{OC}$ ,  $J_{SC}$ , and FF by modulating the cell micro-cavity via appropriately increasing the material's refractive index  $n$ . Our investigation of this unique intrinsic chromatic dispersed reflection not only provides an insight into the nature of organic conjugated materials, but also establishes design principles for optimizing light management of OSC active layers.

## Methods

### Materials

Unless stated otherwise, materials and solvents were commercially obtained. PM6, Y6, D18, N3, L8-BO, P3HT and other conjugated organic small molecules and polymers were purchased from Solmer Materials Inc. All materials were used as received without further purification.

### Reflection measurement

1.5 cm × 1.5 cm size quartz was pre-cleaned with ultrasonic in deionized water, acetone and isopropyl alcohol for three times, 10 min each, then dried with Argon blow. The active layer was spin-coated in air condition from a chloroform (CF) or *o*-dichlorobenzene (*o*-DCB) solution of Y6 (P3HT) which was prepared with the concentration of 10 mg/ml. The thickness of the Y6 (P3HT) active layer was optimized as 40 nm (60 nm). The thermal annealing step was carried out in air, and the annealing temperatures of Y6 and P3HT were 160 °C and 200 °C, respectively. The reflection measurement was performed by a self-built setup which was composed with a Y-shape optical fiber and a grating spectrometer. Finally, the reflection results were revised by a standard Aluminum mirror. To accelerate the speed of the spectrometer, a fast CCD detector is used, which guaranteed that the optical reflection at each wavelength was simultaneously recorded. For each spectrum, the capture time could be tuned towards less than a few milliseconds.

### Refraction measurement

Spectral data below 1.7 μm were measured using an RC2 ellipsometer to obtain the ellipsometric parameters  $\Psi$  and  $\Delta$ . The measurements were performed at angles ranging from 45° to 60° in 5° increments. The dielectric function was extracted by fitting the ellipsometric parameters using a B-Spline oscillator model. For wavelengths above 1.7 μm, an IR-VASE Mark II ellipsometer was used, with measurements taken at 60° and 70° at a resolution of 8 cm<sup>-1</sup>. The dielectric function was obtained by fitting the ellipsometric parameters ( $\Psi$  and  $\Delta$ ) using three Lorentz oscillators. The sample preparation for the ellipsometer measurement are the same as for reflection measurement.

### Device preparation

The conventional devices were fabricated with a structure of glass/ITO/PEDOT:PSS/active layers/PNDIT-F3N/Ag. The ITO-coated glass

substrates were cleaned by ultrasonic treatment in detergent, deionized water, acetone, and isopropyl alcohol under ultrasonication for 15 min each and subsequently dried by a nitrogen blow. A thin layer (~20 nm) of PEDOT:PSS (Clevios P VP Al 4083, filtered at 0.45  $\mu\text{m}$ ) was spin-coated at 4000 rpm onto ITO surface. After baked at 150 °C for 20 min, the substrates were transferred into a nitrogen-filled glove box. Subsequently, the blend solution of PM6:Y6 (1:1.2 w/w, from CF with 0.5% CN), PM6:L8-BO (1:1.2 w/w, from CF with 0.25% DIO) or D18:N3 (1:1 w/w, from CF) was spin-coated to form the active layers with different thicknesses. Then the substrates were TA treatment with 100 °C for 5 min. After that, The ETL solution PNDIT-F3N was spin-coated on the top of active layers at 3000 rpm. Finally, 120 nm Ag layer were deposited under high vacuum ( $<1.5 \times 10^{-4}$  Pa). The effective areas of cells were ~4 mm<sup>2</sup> defined by shallow masks.

The inverted devices were fabricated with a structure of glass/ITO/ZnO/active layer/MoO<sub>3</sub>/Ag. A ZnO sol-gel solution was deposited onto pre-treated ITO-coated glass substrates via spin-coating, followed by annealing on a hotplate at 200 °C for 30 min to form an ~30 nm-thick electron transport layer. Subsequently, a CF solution of the prepared PM6:Y6 blend active layer was spin-coated onto the ZnO layer. By adjusting the concentration and spin speed, thin films with different thicknesses were fabricated, which were then annealed on a hotplate at 100 °C for 5 min. The sample was then transferred into a vacuum deposition chamber, where ~8 nm of MoO<sub>3</sub> and 120 nm of Ag metal electrodes were thermally evaporated sequentially under high vacuum conditions ( $<1.5 \times 10^{-4}$  Pa). The effective areas of cells were ~4 mm<sup>2</sup> defined by shallow masks.

The fabrication process for flexible PM6:Y6 devices was consistent with that of conventional devices, except that the substrate was replaced with ITO-coated PET substrates.

### Device characterization

The *J*-*V* curves of all devices were recorded by a Keithley 2400 source meter and a simulated AM 1.5G (100 mW/cm<sup>2</sup>) solar spectrum generating from LSS-55 solar simulator (50 × 50 mm<sup>2</sup> spot size) of Jinzhu Technology CO., LTD.

The EQE spectral were recorded utilizing spectral response measurement system LST-QE of Jinzhu Technology CO., LTD.

### Ultrafast recombination characterization

Femtosecond transient absorption (fs-TA) spectroscopy (Coherent Legend) was conducted with a wavelength of 800 nm and a laser of 2840 mW (80 MHz, 120 fs) emitted from a seed source through a titanium sapphire amplifier. The laser wavelength is still 800 nm, the pulse is 1000 Hz, the time interval is 120 fs. 30% of the beam is used as the probe enters the transient absorption spectrometer, and the remaining 70% is converted to 400 nm by BBO crystal, which is pumped into the sample as excitation light (400 nm, 1000 Hz, 100 mW). The test section is the visible light region (450–800 nm).

### Transient photovoltage (TPV)/transient photocurrent (TPC)

The TPV and TPC data were acquired with the all-in-one characterization platform Paios (Fluxim AG, Switzerland). In the TPV measurement, the light intensity is in the range of 0.10% to 80.0%, the relative intensity is 20.0%, the stabilization time is 30.0 ms, and the pulse length is 5.0 ms. The TPC of the device was tested under short-circuit conditions without bias light.

### GIWAXS measurement

GIWAXS data were collected at beamline BL14B1 of the Shanghai Synchrotron Radiation Facility (SSRF). The wavelength was 1.2398 Å and the incident angle was 0.12°.

### Reporting summary

Further information on research design is available in the Nature Portfolio Reporting Summary linked to this article.

### Data availability

The authors declare that the source data generated in this study are provided in the Supplementary Information and Source Data file. Source data are provided with this paper.

### References

- Meng, L. X. et al. Organic and solution-processed tandem solar cells with 17.3% efficiency. *Science* **361**, 1094–1098 (2018).
- Li, C. et al. Non-fullerene acceptors with branched side chains and improved molecular packing to exceed 18% efficiency in organic solar cells. *Nat. Energy* **6**, 605–613 (2021).
- Burlingame, Q. et al. Intrinsically stable organic solar cells under high-intensity illumination. *Nature* **573**, 394–397 (2019).
- Ghosh, P. et al. Decoupling excitons from high-frequency vibrations in organic molecules. *Nature* **629**, 355–362 (2024).
- Fabry, C. & Perot, A. Theorie et applications d'une nouvelle methode de spectroscopie interferentielle. *Ann. Chim. Phys.* **16**, 115 (1899).
- Park, M. J. et al. High efficiency red top-emitting micro-cavity organic light emitting diodes. *Opt. Express* **22**, 19919–19929 (2014).
- Wang, J. -Q. et al. Micro-resonant cavity organic light-emitting diode with high refractive index contrast dielectric metasurfaces for naked-eye 3D display. *Opt. Commun.* **532**, 129251 (2023).
- Du, W., Zhang, S., Zhang, Q. & Liu, X. Recent progress of strong exciton-photon coupling in lead halide perovskites. *Adv. Mater.* **31**, 1804894 (2019).
- Al-Saymari, F. A. et al. Resonant cavity enhanced InAs/GaAsSb SLS LEDs with a narrow spectral linewidth and a high-spectral intensity operating at 4.6  $\mu\text{m}$ . *Appl. Phys. Lett.* **123**, 201103 (2023).
- Han, D. et al. Flexible color tunability and high transmittance semitransparent organic solar cells. *Sol. RRL* **6**, 2200441 (2022).
- Cha, S. J., Jeon, J. H. & Suh, M. C. Full color organic light emitting diodes with laser-patterned optical path-length compensation layer. *Org. Electron.* **15**, 2830–2836 (2014).
- Hu, B. et al. 19.5% Efficiency organic solar cells enabled by a direct C-H arylation-derived wide-bandgap small-molecule guest donor. *Energy Environ. Sci.* **17**, 7803–7815 (2024).
- Chen, H. et al. Organic solar cells with 20.82% efficiency and high tolerance of active layer thickness through crystallization sequence manipulation. *Nat. Mater.* **24**, 444–453 (2025).
- Jiang, Y. et al. Non-fullerene acceptor with asymmetric structure and phenyl-substituted alkyl side chain for 20.2% efficiency organic solar cells. *Nat. Energy* **9**, 975–986 (2024).
- Li, C. et al. Non-fullerene acceptors with high crystallinity and photoluminescence quantum yield enable >20% efficiency organic solar cells. *Nat. Mater.* **24**, 433–443 (2025).
- Rao, A. & Friend, R. H. Harnessing singlet exciton fission to break the Shockley-Queisser limit. *Nat. Rev. Mater.* **2**, 17063 (2017).
- Kirchartz, T. & Rau, U. What makes a good solar cell?. *Adv. Energy Mater.* **8**, 1703385 (2018).
- Liu, K. et al. 19.7% efficiency binary organic solar cells achieved by selective core fluorination of nonfullerene electron acceptors. *Joule* **3**, 835–851 (2024).
- Asane, J. K. et al. Stimulated emission in vicinity of the critical angle. *Appl. Phys. Lett.* **119**, 031102 (2021).
- Kerremans, R. et al. The optical constants of solution-processed semiconductors—new challenges with perovskites and non-fullerene acceptors. *Adv. Optical Mater.* **8**, 2000319 (2020).
- Faisst, J. et al. Organic solar cell with an active area > 1 cm<sup>2</sup> achieving 15.8% certified efficiency using optimized VIS-NIR anti-reflection coating. *Sol. RRL* **7**, 2300663 (2023).

22. Xiao, L. et al. Semitransparent organic solar cells with homogeneous transmission and colorful reflection enabled by an ITO-free microcavity architecture. *Adv. Mater.* **36**, 2303844 (2023).
23. Shen, Z. et al. Surface crystallinity enhancement in organic solar cells induced by spinodal demixing of acceptors and additives. *Energy Environ. Sci.* **16**, 2945 (2023).
24. Zhang, J. W. et al. Toward ultra-low reflectance semi-transparent organic photovoltaic cells with biomimetic nanostructured transparent electrode. *Org. Electron.* **60**, 38–44 (2018).
25. Myers, J. D. et al. A universal optical approach to enhancing efficiency of organic-based photovoltaic devices. *Energy Environ. Sci.* **5**, 6900 (2012).
26. Sarkin, A. S., Ekren, N. & Sağlam, S. A review of anti-reflection and self-cleaning coatings on photovoltaic panels. *Sol. Energy* **199**, 63–73 (2020).
27. Pettersson, L. A. A., Roman, L. S. & Inganäs, O. Modeling photocurrent action spectra of photovoltaic devices based on organic thin films. *J. Appl. Phys.* **86**, 487 (1999).
28. Yu, J. D. et al. Composition waves in solution-processed organic films and its propagations from kinetically frozen surface mesophases. *Adv. Funct. Mater.* **33**, 2302089 (2023).
29. Asanov, N., Schopp, N., Valagiannopoulos, C. & Brus, V. Optical and photovoltaic properties of organic solar cells versus bulk-heterojunction morphology. *Phys. Rev. B* **109**, 205201 (2024).
30. Emmott, C. J. M. et al. Organic photovoltaic greenhouses: a unique application for semi-transparent PV?. *Energy Environ. Sci.* **8**, 1317–1328 (2015).
31. Kafle, P. et al. Drastic modulation of molecular packing and intrinsic dissolution rates by meniscus-guided coating of extremely confined pharmaceutical thin films. *ACS Appl. Mater. Interfaces* **13**, 56519–56529 (2021).
32. Qu, G. et al. Lyotropic liquid crystalline mesophase governs interfacial molecular orientation of conjugated polymer thin films. *Chem. Mater.* **32**, 6043–6054 (2020).
33. Xu, Z. et al. Not all aggregates are made the same: distinct structures of solution aggregates drastically modulate assembly pathways, morphology, and electronic properties of conjugated polymers. *Adv. Mater.* **34**, 2203055 (2022).
34. te Velde, G. Chemistry with ADF. *J. Comput. Chem.* **22**, 931–967 (2001).
35. Guerra, C. F., Snijders, J. G., Velde, te, G. & Baerends, E. J. Towards an order-*N* DFT method. *Theor. Chem. Acc.* **99**, 391–403 (1998).
36. Jensen, L., Autschbach, J. & Schatz, G. C. Finite lifetime effects on the polarizability within time-dependent density-functional theory. *J. Chem. Phys.* **122**, 224115 (2005).
37. Jensen, L., Zhao, L. L., Autschbach, J. & Schatz, G. C. Theory and method for calculating resonance Raman scattering from resonance polarizability derivatives. *J. Chem. Phys.* **123**, 174110 (2005).
38. Pachucki, K. & Puchalski, M. P. Refractive index and generalized polarizability. *Phys. Rev. A* **99**, 041803 (2019).
39. Yao, H. F. & Hou, J. H. Recent advances in single-junction organic solar cells. *Angew. Chem. Int. Ed.* **61**, e202209021 (2022).
40. Xiao, Y. et al. Unveiling the crystalline packing of Y6 in thin films by thermally induced “backbone-on” orientation. *J. Mater. Chem. A* **9**, 17030–17038 (2021).
41. Zhang, G. et al. Delocalization of exciton and electron wavefunction in non-fullerene acceptor molecules enables efficient organic solar cells. *Nat. Commun.* **11**, 3943 (2020).
42. O’Connor, B. et al. Anisotropic structure and charge transport in highly strain-aligned regioregular poly(3-hexylthiophene). *Adv. Funct. Mater.* **21**, 3697–3705 (2011).
43. Sun, F. et al. 1,5-Diiodocyclooctane: a cyclane solvent additive that can extend the exciton diffusion length in thick film organic solar cells. *Energy Environ. Sci.* **17**, 1916–1930 (2024).
44. Wang, J. X. et al. Synergetic strategy for highly efficient and super flexible thick-film organic solar cells. *Adv. Energy Mater.* **12**, 2201614 (2022).
45. Zou, B. S. et al. Step-by-step modulation of crystalline features and exciton kinetics for 19.2% efficiency ortho-xylene processed organic solar cells. *Nano-Macro Lett.* **16**, 30 (2024).
46. Azzouzi, M. et al. Reconciling models of interfacial state kinetics and device performance in organic solar cells: impact of the energy offsets on the power conversion efficiency. *Energy Environ. Sci.* **15**, 1256 (2022).
47. Liang, S. et al. Efficient hole transfer via delocalized excited state in small molecular acceptor: a comparative study on photodynamics of PM6:Y6 and PM6:ITIC organic photovoltaic blends. *Adv. Funct. Mater.* **31**, 2102764 (2021).
48. Duan, X. P. et al. Ternary strategy enabling high-efficiency rigid and flexible organic solar cells with reduced non-radiative voltage loss. *Energy Environ. Sci.* **15**, 1563–1572 (2022).
49. Li, X. Y. et al. Benzotriazole-based 3D four-arm small molecules enable 19.1% efficiency for PM6: Y6-based ternary organic solar cells. *Angew. Chem. Int. Ed.* **62**, 2306847 (2023).
50. Zhang, Y. et al. Achieving 19.4% organic solar cell via an in-situ formation of p-i-n structure with built-in interpenetrating network. *Joule* **8**, 509–526 (2024).
51. Liu, Y. & Russell, T. P. Electroactive ionenes: efficient interlayer materials in organic photovoltaics. *Acc. Chem. Res.* **55**, 1097–1108 (2022).
52. Sun, B., Gerber, B., Shoaee, S. & Neher, D. An analytical model for describing transient photocurrents in bias-assisted charge extraction for low-mobility organic solar cells. *Sol. RRL* **8**, 2400211 (2024).
53. Alam, S. et al. Thermally-induced degradation in PM6:Y6-based bulk heterojunction organic solar cells. *Adv. Funct. Mater.* **34**, 2308076 (2024).
54. Ghorab, M., Fattah, A. & Joodaki, M. Fundamentals of organic solar cells: a review on mobility issues and measurement methods. *Optik* **267**, 169730 (2022).
55. Zhang, T. et al. Suppressing the energetic disorder of all-polymer solar cells enables over 18% efficiency. *Energy Environ. Sci.* **16**, 1581 (2023).
56. Brus, V. V. et al. Capacitance spectroscopy for quantifying recombination losses in non-fullerene small-molecule bulk heterojunction solar cells. *Adv. Energy Mater.* **6**, 1502250 (2016).
57. Xie, L. et al. Modulation of crystallization kinetics using a guest acceptor for high-performance organic solar cells with 19.8% efficiency. *Energy Environ. Sci.* **17**, 7838–7849 (2024).
58. Wei, Y. A. et al. Binary organic solar cells breaking 19% via manipulating the vertical component distribution. *Adv. Mater.* **34**, 2204718 (2022).
59. Weng, K. et al. Optimized active layer morphology toward efficient and polymer batch insensitive organic solar cells. *Nat. Commun.* **11**, 2855 (2020).
60. Gondek, E. Optical optimization of organic solar cell with bulk heterojunction. *Opto-Electron. Rev.* **22**, 77–85 (2014).
61. Guan, S. T. et al. Self-assembled interlayer enables high-performance organic photovoltaics with power conversion efficiency exceeding 20%. *Adv. Mater.* **36**, 2400342 (2024).
62. Cai, Y. H. et al. Vertically optimized phase separation with improved exciton diffusion enables efficient organic solar cells with thick active layers. *Nat. Commun.* **13**, 2369 (2020).
63. Shen, Z. et al. Film-depth-dependent light reflection spectroscopy for photovoltaics and transistors. *Adv. Mater. Interfaces* **8**, 2101476 (2021).
64. Zhu, H. et al. Boosting performance of self-powered near-infrared organic spectral detector through metal-dielectric microcavity. *Adv. Opt. Mater.* **12**, 2301575 (2024).

65. Zhao, Z. et al. Photomultiplication type broad response organic photodetectors with one absorber layer and one multiplication layer. *J. Phys. Chem. Lett.* **11**, 366–373 (2020).
66. Chen, Z. Y. et al. Isomerization strategy on a non-fullerene guest acceptor for stable organic solar cells with over 19% efficiency. *Energy Environ. Sci.* **16**, 3119–3127 (2023).
67. Ye, Q. R. et al. Ductile oligomeric acceptor-modified flexible organic solar cells show excellent mechanical robustness and near 18% efficiency. *Adv. Mater.* **35**, 2305562 (2023).
68. Cheng, C. J. et al. Device engineering of non-fullerene organic photovoltaics with extrapolated operational T 80 lifetime over 45,000 h in air. *Joule* **8**, 2250–2264 (2024).
69. Guo, C. H. et al. A polycrystalline polymer donor as pre-aggregate toward ordered molecular aggregation for 19.3% efficiency binary organic solar cells. *Adv. Mater.* **35**, 2304921 (2023).
70. Ma, L. et al. Morphology control by tuning electrostatic interactions for efficient polythiophene-based all-polymer solar cells. *Chem* **9**, 2518–2529 (2023).
71. Go, E. et al. Spectrally resolved exciton polarizability for understanding charge generation in organic bulk hetero-junction diodes. *J. Am. Chem. Soc.* **146**, 14724–14733 (2024).

## Acknowledgements

G.L. thanks the National Natural Science Foundation of China (Grants No. 52273026). L.M. thanks the National Natural Science Foundation of China (Grants Nos. 52203245 and 52473198), the China Postdoctoral Innovative Talent Support Program (BX 20220274), and Henan Provincial Science and Technology Research and Development Program Joint Fund (232301420034). The authors thank Dr. Huirong Su from Genuine Optronics Limited for providing ellipsometer measurement. The authors thank the Shanghai Synchrotron Radiation Facility for providing GIWAXS measurements. The authors extend their gratitude to Jiangkun Liu from hengquwang Platform ([www.hengquwang.com](http://www.hengquwang.com)) for providing invaluable assistance with the fs-TA analysis.

## Author contributions

Z.S. performed part of the experiment and simulation, and wrote the manuscript. G.L. (Guanyu Lu), X.C. and X.T. mainly contributed to the simulation part. S.L., Y.Z. (Yuanyuan Zhang), J.W. and L.M. designed and fabricated the OSCs devices. J.Y., Y.Z. (Yuanwei Zhu), F.G. gave the experiment assistance. G.L. (Guanghao Lu), L.B., Y.Z. (Yuanwei Zhu) and H.P. provided some insightful discussions. The manuscript was written

through contributions of all authors. All authors have given approval to the final version of the manuscript.

## Competing interests

The authors declare no competing interests.

## Additional information

**Supplementary information** The online version contains supplementary material available at <https://doi.org/10.1038/s41467-025-67379-z>.

**Correspondence** and requests for materials should be addressed to Yuanwei Zhu, Hongge Pan, Lingxian Meng or Guanghao Lu.

**Peer review information** *Nature Communications* thanks Xinhui Lu who co-reviewed with Yuang Fu, and the other, anonymous, reviewer(s) for their contribution to the peer review of this work. A peer review file is available.

**Reprints and permissions information** is available at <http://www.nature.com/reprints>

**Publisher's note** Springer Nature remains neutral with regard to jurisdictional claims in published maps and institutional affiliations.

**Open Access** This article is licensed under a Creative Commons Attribution-NonCommercial-NoDerivatives 4.0 International License, which permits any non-commercial use, sharing, distribution and reproduction in any medium or format, as long as you give appropriate credit to the original author(s) and the source, provide a link to the Creative Commons licence, and indicate if you modified the licensed material. You do not have permission under this licence to share adapted material derived from this article or parts of it. The images or other third party material in this article are included in the article's Creative Commons licence, unless indicated otherwise in a credit line to the material. If material is not included in the article's Creative Commons licence and your intended use is not permitted by statutory regulation or exceeds the permitted use, you will need to obtain permission directly from the copyright holder. To view a copy of this licence, visit <http://creativecommons.org/licenses/by-nc-nd/4.0/>.

© The Author(s) 2025